Phase Transition Dynamics in a Complex Oxide Heterostructure

Qingteng Zhang (张庆腾),[1,*] Guoxiang Hu (胡国香),[2,3,*] Vitalii Starchenko,[4,*] Gang Wan,[5,¶] Eric M. Dufresne,[1] Yongqi Dong,[5] Huajun Liu,[6] Hua Zhou,[1] Hyoungjeen Jeen,[7] Kayahan Saritas,[7] Jaron T. Krogel,[7] Fernando A. Reboredo,[7] Ho Nyung Lee,[7] Alec R. Sandy,[1] Irene Calvo Almazan,[5,§] Panchapakesan Ganesh,[2,†] and Dillon D. Fong[5,‡]

[1]*X-Ray Science Division, Argonne National Laboratory, Lemont, Illinois 60439, USA*
[2]*Center for Nanophase Materials Sciences, Oak Ridge National Laboratory, Oak Ridge, Tennessee 37831, USA*
[3]*Department of Chemistry and Biochemistry, Queens College, City University of New York, Queens, New York 11367, USA*
[4]*Chemical Sciences Division, Oak Ridge National Laboratory, Oak Ridge, Tennessee 37831, USA*
[5]*Material Science Division, Argonne National Laboratory, Lemont, Illinois 60439, USA*
[6]*Institute of Materials Research and Engineering, A*STAR, Singapore, 138634, Singapore*
[7]*Materials Science and Technology Division, Oak Ridge National Laboratory, Oak Ridge, Tennessee 37831, USA*

(Received 8 June 2022; revised 29 August 2022; accepted 5 October 2022; published 30 November 2022)

Understanding the behavior of defects in the complex oxides is key to controlling myriad ionic and electronic properties in these multifunctional materials. The observation of defect dynamics, however, requires a unique probe—one sensitive to the configuration of defects as well as its time evolution. Here, we present measurements of oxygen vacancy ordering in epitaxial thin films of $SrCoO_x$ and the brownmillerite-perovskite phase transition employing x-ray photon correlation spectroscopy. These and associated synchrotron measurements and theory calculations reveal the close interaction between the kinetics and the dynamics of the phase transition, showing how spatial and temporal fluctuations of heterointerface evolve during the transformation process. The energetics of the transition are correlated with the behavior of oxygen vacancies, and the dimensionality of the transformation is shown to depend strongly on whether the phase is undergoing oxidation or reduction. The experimental and theoretical methods described here are broadly applicable to *in situ* measurements of dynamic phase behavior and demonstrate how coherence may be employed for novel studies of the complex oxides as enabled by the arrival of fourth-generation hard x-ray coherent light sources.

DOI: 10.1103/PhysRevLett.129.235701

The manipulation of correlated electron oxides has remarkable potential for the development of ionotronic devices [1–5]. Reversible metal-to-insulator transitions are possible, for example, via ionic liquid gating [6–9] or by other chemical and electrochemical means [10–14]. Such transitions rely on fundamental changes triggered by oxygen incorporation or excorporation and migration [15], and the surrounding environment plays a critical role in both the intrinsic properties and phase reversibility [16–18]. Two members of the strontium cobaltite family of complex oxides stand out as materials useful for memristive applications [19,20] as they exhibit a large reversible change, transitioning from an insulating, antiferromagnetic phase—brownmillerite $SrCoO_{2.5}$—to a metallic, ferromagnetic phase—perovskite $SrCoO_3$—a change of 0.5 oxygens per formula unit (∼17%). In such defect ordered systems, the resistance state can be tuned as there is expected to be strong interplay between the individual defects, the strain state, and the behavior of the order-disorder phase boundary. In a recent experimental study of $SrCoO_x$ thin films, it was shown that unstrained films undergo spontaneous reduction owing to the large positive Gibbs free energy of the perovskite (PV) phase with respect to the brownmillerite (BM) phase [21]. High-resolution scanning transmission electron microscopy measurements conducted either under applied bias [22] or during ionic liquid gating [23] have also revealed important structural aspects of the transition process such as the significant impact of crystalline anisotropy on the boundary velocity. For a variety of reasons, however, detailed studies concerning both the kinetics and dynamics of the transition between the ordered oxygen-phase to the ordered vacancy phase have yet to be explored.

Here we describe an investigation of the phase transition in a $SrCoO_x/SrTiO_3$ (001) heterostructure, exploiting the coherence of a third-generation synchrotron and wide-angle x-ray photon correlation spectroscopy (XPCS). The BM and PV crystal structures are shown in Fig. 1(a). As depicted, the perovskite crystal structure can be considered a network of interconnected oxygen octahedra with Co at their centers and Sr cations between them. In the brownmillerite crystal structure, the network is comprised of both octahedral and tetrahedral layers in an alternating sequence along the out-of-plane (z) direction. As we and others have

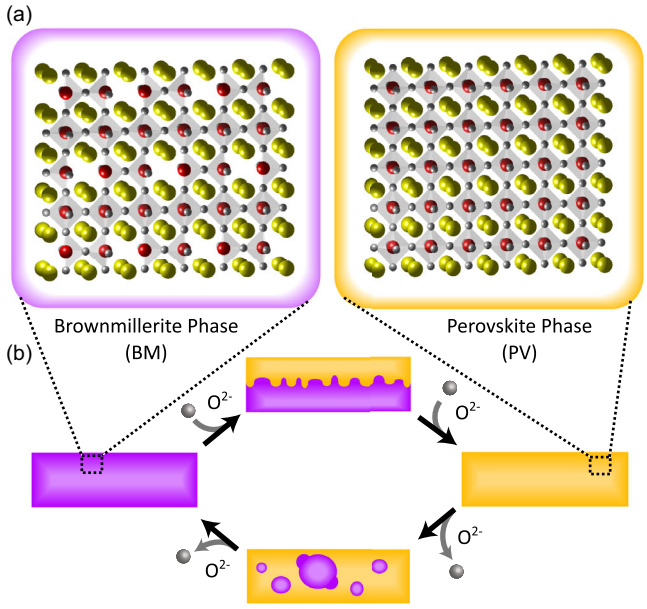

FIG. 1. (a) Cross sections of the BM (violet box) and PV (orange box) crystal structures in $SrCoO_x$. The red, yellow, and gray atoms refer to Co, Sr, and O, respectively. (b) Schematics of the oxidization (BM → PV) and reduction (PV → BM) processes during the topotactic phase transition in the $SrCoO_x$ thin film.

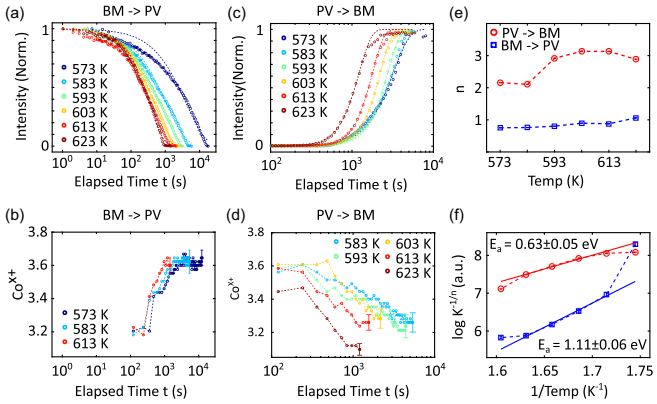

FIG. 2. Kinetics of oxidation and reduction. (a) Normalized intensity of the $00\frac{1}{2}$ reflection for a $SrCoO_x/SrTiO_3$ (001) heterostructure during the oxidization process. The time zero corresponds to the time where the atmosphere is switched from N_2 to O_2. The dashed lines are fits using the Johnson-Mehl-Avrami equation [Eq. (1)]; (b) XANES measurements under the same experimental conditions as (a). For clarity, only the error bar of the last point is displayed. (c) Normalized intensity of the $00\frac{1}{2}$ reflection during the reduction process. (d) XANES measurements under the same experimental conditions as (c). (e) Temperature dependence of the dimensionality n from fitting of Johnson-Mehl-Avrami equation [Eq. (1)] for both oxidization and reduction processes. (f) Temperature dependence of the characteristic time ($K^{-1/n}$) and the activation energy (E_a) for the phase growth from the same fitting. The error bars are smaller than the size of the markers.

shown, the transition between the two phases is topotactic in nature, i.e., the new lattice is crystallographically related to that of the original, preserving the overall crystal shape during the transition [17]. Importantly for this experiment, the PV and BM phases are also similar in lattice parameter such that both remain (001)-oriented and coherently strained with the $SrTiO_3$ (001) substrate throughout the phase transition, and the transition can take place repeatedly without any observable deterioration in film quality as shown in Fig. S1(a) [24]. Since the PV to BM phase transition causes doubling of the unit cell size along z, this leads to the formation of half-order reflections in reciprocal space, e.g., $00\frac{1}{2}$ r.l.u., $00\frac{3}{2}$ r.l.u., etc., where r.l.u. refers to reciprocal lattice units based on the $SrTiO_3$ lattice parameter (0.3905 nm). While the kinetics of the transition can be monitored by changes to the integrated intensity of these reflections, the XPCS experiment requires use of the coherent portion of the incident x-ray beam: this was selected by passing the beam through a monochromator and a series of slits with the size of the slits set to match the transverse coherence length of the x rays. Coherent scattering ("speckle") from the tail of the BM peak can be observed at both the Bragg peak and the 1st thickness fringe [Figs. S1(b) and S1(c), respectively [24]]. X-ray absorption near-edge spectroscopy (XANES) at the Co K edge was also measured, providing information on the oxygen vacancy concentration regardless of the crystal structure.

After synthesis, the strontium cobaltite is in the BM phase [17]. When the environment is switched from an inert environment (N_2) to an oxidizing environment (O_2) at elevated temperatures (at $t = 0$ in Fig. 2), the BM surface dissociates the O_2 molecule, allowing oxygen to enter the film and fill oxygen vacancies near the film surface. From the x-ray measurements, one can readily observe when oxygen starts to enter the lattice. The integrated intensity of the $00\frac{1}{2}$ reflection begins to decay immediately, as shown in Fig. 2(a), with the slowest change occurring at 573 K and fastest at 613–623 K. Interestingly, the XANES results presented in Fig. 2(c) shows that it generally takes longer than 100 sec before the average Co oxidation state begins to change, suggesting that the oxygen vacancy structure in the BM phase disorders very quickly. Furthermore, after the disappearance of the $00\frac{1}{2}$ reflection, the final stoichiometry is approximately $SrCoO_{2.8}$, with the film containing slightly less oxygen at the higher temperatures. This is in general agreement with the overall properties of $SrCoO_x$ which favors the BM phase over the PV phase when coherently strained to $SrTiO_3$ (001) [17].

Regarding the reduction process, i.e., when the environment is switched from O_2 to N_2, the perovskite phase does not lose oxygen immediately [Fig. 2(d)], and vacancy ordering displays considerable incubation time [Fig. 2(b)]. This suggests that the kinetics of oxygen vacancy ordering plays a key role during the PV to BM transition. The temperature dependence is also considerable, taking < 200 sec to reach $SrCoO_{2.75}$ at 623 K and ~1000 sec at 583 K.

This is partially due to less oxygen in the initial condition ($x \sim 2.8$ at 573 K and 2.76 at 623 K). Complete reduction back to $x = 2.5$ may take > 104 sec at lower temperatures. Regarding the BM to PV transition, 50% of the $00\frac{1}{2}$ intensity is reached at ~2500 sec at 573 K, while taking only 1000 sec at 623 K. This temperature dependence is indicative of the low activation energy for oxygen ion diffusion.

The growth of PV and BM phases during the oxidization and reduction processes can be well described using the Johnson-Mehl-Avrami equation,

$$Y = 1 - \exp(-Kt^n), \tag{1}$$

where Y is the ratio of the volume of the growing phase to that of the entire film. Here, nucleation of the new phase is assumed to occur randomly throughout the volume of the film with a growth rate independent of the extent of the transformation. We performed fits to Eq. (1) in regions of Figs. 2(a) and 2(c) where the normalized intensity of the BM phase was between 0 and 0.8 to focus on stages with the highest growth rate: the results for n and $\log(K^{-1/n})$ are shown in Figs. 2(e) and 2(f), respectively. The variable n describes the dimensionality of the growing of the phase, and the quantity $K^{-1/n}$ is a dimension-independent characteristic time that corresponds to the time it takes for the phase to grow to $1 - 1/e$ of the total volume. It can be seen in Fig. 2(e) that the dimensionality of PV growth into the BM phase remains close to 1 during the oxidization process but varies between 2 and 3 during the reduction process. Within the temperature range of 583 to 613 K, an activation energy E_a of 1.11 ± 0.06 eV is extracted for the oxidization process and 0.63 ± 0.05 eV for the reduction process [dashed lines in Fig. 2(f)]. This is in accord with results from first-principles simulations (details in Supplemental Material [24]) that provide a more rigorous description of the underlying atomistic processes. Briefly, oxidation from BM → PV involves a vacancy-interstitial mechanism of diffusion along the layering direction into the BM phase after surface dissociation of oxygen dimers, with an activation energy of 1.03 eV. Reduction from PV → BM involves an initial incubation process due to vacancy short-range ordering but eventually proceeds via 3D single-vacancy migration with an activation energy of 0.46–0.67 eV depending on the strain state of the $SrCoO_x$ film.

The topotactic phase transition, as depicted by the schematic in Fig. 1, involves changes in the relative amounts of the BM and PV phases, reflecting the kinetics of the transition. However, there are also changes at a local level as some nuclei grow while others shrink: these fluctuations are driven by hopping of the system among energetically degenerate metastable states with different structural configurations [54] and can occur on very different timescales from the kinetics, as was observed for other domain-forming condensed matter systems [55–59]. Such spatial rearrangements usually occur within the coherence length, i.e., the scale at which the BM/PV phase remains ordered, here estimated by the full-width-half-maximum of the Bragg peak. In this Letter, the fluctuation dynamics, as characterized by the temporal decorrelation of coherently scattered intensities, were measured with XPCS and analyzed using the two-time correlation function (Supplemental Material [24], Figs. S2 and S3). As depicted in Fig. 3(a) for $SrCoO_x/SrTiO_3$, the environment was switched from N_2 to O_2 at time zero, here for a temperature of 603 K. Prior to the switch at time zero, the correlation remains high, which suggests that the spatial configuration of the BM phase is static in the absence of the PV phase, and the dynamics that occur after time zero mainly arise from fluctuations of the phase boundaries between the BM and the PV phases. This can be more easily seen by the horizontal cuts, A, B, and C, presented as a function of logarithmic time in Fig. 3(b). Here, the dashed horizontal line (black) corresponds to half of the maximum correlation, with the intersection between the line and the experimental data yielding τ_C, a characteristic time representing the timescale of the phase fluctuations dependent on both phase propagation at longer time scales and phase fluctuations at shorter timescales. While Fig. 2 provides information on the kinetics of the phase transition as well as changes to the oxidation state, the behavior of two-time correlation function provides information on fluctuations in the spatial configuration of the coexisting and competing phases. As shown at the bottom of Fig. 3(c), when at 184 sec into the transformation (point A), the majority of the film is still in the BM phase and configurations measured every 30 sec apart are very similar, as indicated by the high correlation at the first point of horizontal cut A in Fig. 3(b) and the color scale in Fig. 3(a). In addition, as shown in Fig. 2(e), the transformation is one-dimensional, with the new PV phase (orange) growing at the expense of the BM phase (violet). As the PV phase continues to propagate from the top surface of the sample into the film, fluctuations at the heterointerface accelerate with time, accompanied by the decrease of the correlation length of the BM phase, L_{BM}. The large spatial variation of the BM-PV boundaries at shorter timescales is predominantly caused by fluctuations at the BM-PV boundaries rather than phase propagation and indicate that local regions vary rapidly between the BM and PV phases as a result of oxygen ion diffusion. Similar trends were observed at all temperatures considered in the Letter (Fig. S3 [24]). At longer timescales (~1000 sec), the configurations are completely decorrelated, suggested by the fact that the correlation falls to 0 in regions sufficiently far from the diagonal. The two-time correlation map thus shows that regions close to the interfacial front switch back and forth between the PV and BM phases, with the configuration of

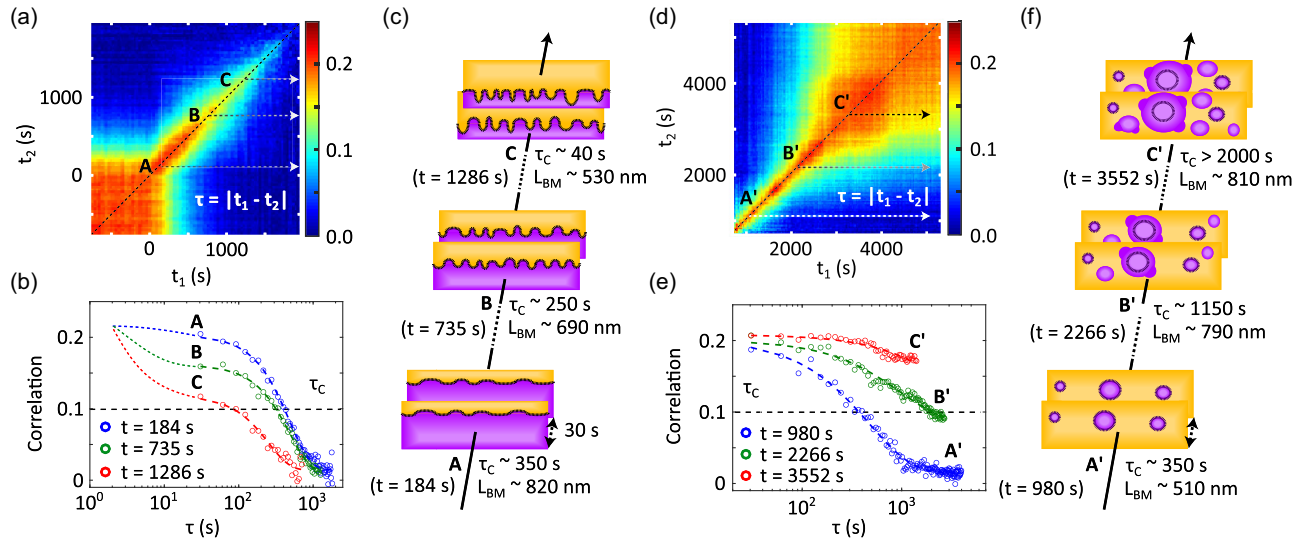

FIG. 3. XPCS analysis of oxidation and reduction processes at 603 K. Two-time correlation maps are shown in (a) and (d) for oxidation and reduction processes, respectively, where A, B, and C and A', B', C' indicate three representative stages during the oxidation and reduction processes, respectively. Note that the time scale in (d) begins at ~900 s. 1D correlation plots of the three representative stages are shown in (b) for oxidation and (e) for reduction. The black dashed lines are for visual identification of the characteristic time τ_C for the phase fluctuation. Schematic illustrations of the topotactic transitions are shown in (c) for the BM to PV phase and in (f) for the PV to BM phase.

the PV phase within the BM matrix fluctuating much more slowly when the volume fraction of PV is small.

Additional insight regarding the PV/BM phase transition can be gained from numerical analysis of the correlation functions. First of all, the correlation function can be very well described using a compressed exponential function $g_2 = g_{2,0}\exp[-2(\tau/\tau_0)^{\beta}] + g_{2,\infty}$ with $\beta = 1.5$, which is usually associated with jamming, i.e., the collective microscopic motion observed during the relaxation of spatially heterogeneous stress [60], as seen in various "hard" and "soft" condensed matter systems [54,61,62]. Jamming during oxidation likely arises from the well-known constrained 1D motion of oxygen ions [63,64]. Second, the highest correlation time that can be observed within the time resolution of the experimental method (30 sec) decreases from stage A to stage C [Fig. 3(c)], indicating that there is likely much faster dynamics with timescales well beyond our measurement [dotted curves in Fig. 3(b)]. In the near future, it will be possible to capture the rapid fluctuations of BM/PV phases as enabled by high-frame-rate, single photon counting x-ray detectors [65,66] and the vast increase in coherent flux available at fourth generation synchrotrons [61,67,68].

Figure 3(d) shows the two-time correlation coefficient during the reduction process at 603 K. Note that time zero corresponds to the moment when the atmosphere is switched from O_2 to N_2; there is no intensity at the $00\frac{1}{2}$ until roughly 600 sec after the N_2 switch. As seen in Fig. 3(d), the fluctuational dynamics accelerates and L_{BM} increases as the reduction process progresses. A similar trend was observed for all temperatures considered in this Letter (Fig. S4 [24]). From the Avrami analysis described above, the PV to BM transformation is more three-dimensional, as depicted in Fig. 3(f). The increase in decorrelation time τ_C with growth of the BM phase is consistent with "aging" of the fluctuations of the BM growth front, which has been observed to occur during phase formation in many other solid condensed matter systems including binary alloys, metallic glasses, and charge density wave domains [69–71]. An important consequence of aging is the partial correlation of the BM phase front over longer temporal separations, as indicated by the rise of the correlation baseline at the end of the measurement. Surprisingly, we find that $\beta = 1$ in $g_2 = g_{2,0}\exp[-2(\tau/\tau_0)^{\beta}] + g_{2,\infty}$ [dashed curves in Fig. 3(e)], similar to the free diffusion seen in the Brownian motion of nanoparticles instead of $\beta = 1.5$, which is typical for jammed states during aging and in the oxidation process shown in Fig. 3(b). A possible explanation is that the vacancies, once they are not trapped to form short-ranged clusters, can diffuse freely in the 3D oxygen network of the PV phase.

Another aspect of the dynamics during the reduction process is the incubation time, which is also seen in Fig. 2(b) where the oxygen-deficient PV phase starts to arrange into the BM phase with ordered oxygen vacancies, as suggested by the DFT calculations described in the Supplemental Material [24]. These early BM phase structures then act as nucleation sites for 3D growth of the BM phase as depicted in Fig. 3(f). An important implication of the dynamics from XPCS is that due to the lack of phase boundary fluctuations during reduction, regions with an established BM phase will not go back to the PV phase.

In other words, during the reduction process, oxygen ions always move away from regions with established vacancy ordered structures, and the motion of the BM-PV phase boundary is driven predominantly by the propagation of the BM phase: this is as if excessive oxygen in the PV phase is "forced out" of the $SrCoO_x$ film by the formation of the BM phase. This physical picture is also consistent with the aging behavior at longer timescales as previously discussed.

Although the dynamics of light ions such as oxygen are difficult to track directly, the oxygen-deficient BM phase is characterized by the unit cell doubling from ordered oxygen vacancies, and the effect of oxygen diffusion is therefore manifested by the change in the intensity of the lattice half-order Bragg reflections. We have shown that during oxidation, oxygen molecules break down into ions, fill vacancies at the top of the brownmillerite phase, and then diffuse into the bulk of the film. The oxygen-rich PV phase propagates in a 1D, top-down manner, and there are significant fluctuations at the BM-PV phase boundary due to the diffusive nature of the oxygen dynamics. During reduction, oxygen vacancies form inside the PV phase and assemble into BM nuclei via the migration of vacancies into an ordered arrangement. The BM phase then expands in a 3D manner, driving excess oxygen out of the film with little fluctuation of the phase boundary in the process. The framework presented in this Letter, namely, the dynamics of light ions probed at signature Bragg reflections using both *in situ* x-ray diffraction (i.e., a spatial average) and coherent x-ray scattering (i.e., variation of the spatial configuration), can be generally applied to analog, memristive synapses and other application-motivated ion-insertion devices and systems such as lithium batteries, fuel cells, and ionic liquid gating [72].

While the time resolution of the XPCS measurements suffices for current Letter, the development of ultrafast photon-counting pixel-array detectors [73,74] and the $100\times$ increase in coherent flux from diffraction-limited synchrotron storage rings and state-of-the-art fast photon-counting pixel-array detectors will allow a wealth of new opportunities with regard to *in situ* and *operando* measurements. In addition to bringing improved time resolution, it is expected that the ability to perform XPCS will become possible and perhaps regularly performed at many experimental stations. This will facilitate studies of highly local behavior such that the statistics of small systems can be compared to those of the larger ensembles. Such capabilities will undoubtably impact the field of complex oxide heterostructures, particularly with regard to improved defect manipulation by local fields and electrochemical means.

Work on the sample and QMC calculations was supported by U.S. Department of Energy, Office of Science, Basic Energy Sciences, Materials Sciences and Engineering Division. V. S. was supported by the U.S. Department of Energy, Office of Science, Basic Energy Sciences, Chemical Sciences, Geosciences, and Biosciences Division. G. H., P. G., and J. T. K. were supported by the U.S. Department of Energy, Office of Science, Basic Energy Sciences, Materials Sciences and Engineering Division, as part of the Computational Materials Sciences Program at the Center for Predictive Simulation of Functional Materials. The x-ray measurements were performed at beam line 8-ID-E of the Advanced Photon Source, a U.S. Department of Energy Office of Science User Facility operated for the DOE Office of Science by Argonne National Laboratory under Contract No. DE-AC02-06CH11357. A portion of research (DFT) was conducted at the Center for Nanophase Materials Sciences, which is a DOE Office of Science User Facility. The QMC calculations used resources of the Oak Ridge Leadership Computing Facility at the Oak Ridge National Laboratory, which is supported by the Office of Science of the U.S. Department of Energy under Contract No. DE-AC05-00OR22725. The DFT calculations used resources of the National Energy Research Scientific Computing Center (NERSC), a U.S. Department of Energy Office of Science User Facility located at Lawrence Berkeley National Laboratory, operated under Contract No. DE-AC02-05CH11231.

[*]These authors contributed equally to this Letter.
[†]ganeshp@ornl.gov
[‡]fong@anl.gov
[§]Present address: Institute of Nanoscicences and Materials of Aragon (INMA), University of Zaragoza Pedro Cerbuna street 12, 50009, Zaragoza, Spain.
[¶]Present address: Department of Mechanical Engineering, Stanford University, Stanford, California 94305, USA.

[1] D. D. Fong and S. Ramanathan, APL Mater. **5**, 042201 (2017).
[2] H.-T. Zhang, Z. Zhang, H. Zhou, H. Tanaka, D. D. Fong, and S. Ramanathan, Adv. Phys. **4**, 1523686 (2019).
[3] H.-T. Zhang, P. Panda, J. Lin, Y. Kalcheim, K. Wang, J. W. Freeland, D. D. Fong, S. Priya, I. K. Schuller, S. K. R. S. Sankaranarayanan, K. Roy, and S. Ramanathan, Appl. Phys. Rev. **7**, 011309 (2020).
[4] P. Ganesh, F. Lechermann, I. Kylänpää, J. T. Krogel, P. R. C. Kent, and O. Heinonen, Phys. Rev. B **101**, 155129 (2020).
[5] M. Chandler Bennett *et al.*, Phys. Rev. Research **4**, L022005 (2022).
[6] Y. Dong, H. Xu, Z. Luo, H. Zhou, D. D. Fong, W. Wu, and C. Gao, APL Mater. **5**, 051101 (2017).
[7] H. Liu, Y. Dong, M. J. Cherukara, K. Sasikumar, B. Narayanan, Z. Cai, B. Lai, L. Stan, S. Hong, M. K. Y. Chan, S. K. R. S. Sankaranarayanan, H. Zhou, and D. D. Fong, ACS Nano **12**, 4938 (2018).
[8] A. T. Bollinger, Z.-B. Wu, L. Wu, X. He, I. Drozdov, J. Wu, I. Robinson, and I. Božović, J. Supercond. Novel Magn. **33**, 93 (2020).
[9] W. Li, J. Shi, K. H. L. Zhang, and J. L. MacManus-Driscoll, Mater. Horiz. **7**, 2832 (2020).

[10] O. T. Tambunan, K. J. Parwanta, S. K. Acharya, B. W. Lee, C. U. Jung, Y. S. Kim, B. H. Park, H. Jeong, J.-Y. Park, M. R. Cho, Y. D. Park, W. S. Choi, D.-W. Kim, H. Jin, S. Lee, S. J. Song, S.-J. Kang, M. Kim, and C. S. Hwang, Appl. Phys. Lett. **105**, 063507 (2014).

[11] Q. Lu and B. Yildiz, Nano Lett. **16**, 1186 (2016).

[12] S. Hu and J. Seidel, Nanotechnology **27**, 325301 (2016).

[13] J. Guo, B. Legum, B. Anasori, K. Wang, P. Lelyukh, Y. Gogotsi, and C. A. Randall, Adv. Mater. **30**, e1801846 (2018).

[14] Q. Lu, C. Sohn, G. Hu, X. Gao, M. F. Chisholm, I. Kylänpää, J. T. Krogel, P. R. C. Kent, O. Heinonen, P. Ganesh, and H. N. Lee, Sci. Rep. **10**, 1 (2020).

[15] F. Gunkel, D. V. Christensen, Y. Z. Chen, and N. Pryds, Appl. Phys. Lett. **116**, 120505 (2020).

[16] C. M. Folkman, S. H. Chang, H. Jeen, E. Perret, P. M. Baldo, C. Thompson, J. A. Eastman, H. N. Lee, and D. D. Fong, APL Mater. **7**, 081126 (2019).

[17] H. Jeen, W. S. Choi, M. D. Biegalski, C. M. Folkman, I.-C. Tung, D. D. Fong, J. W. Freeland, D. Shin, H. Ohta, M. F. Chisholm, and H. N. Lee, Nat. Mater. **12**, 1057 (2013).

[18] W. S. Choi, H. Jeen, J. H. Lee, S. S. Ambrose Seo, V. R. Cooper, K. M. Rabe, and H. N. Lee, Phys. Rev. Lett. **111**, 097401 (2013).

[19] X. Mou, J. Tang, Y. Lyu, Q. Zhang, S. Yang, F. Xu, W. Liu, M. Xu, Y. Zhou, W. Sun, Y. Zhong, B. Gao, P. Yu, H. Qian, and H. Wu, Sci. Adv. **7**, eabh0648 (2021).

[20] S. Zhang and G. Galli, npj Comput. Mater. **6**, 170 (2020).

[21] J. R. Petrie, C. Mitra, H. Jeen, W. S. Choi, T. L. Meyer, F. A. Reboredo, J. W. Freeland, G. Eres, and H. N. Lee, Adv. Funct. Mater. **26**, 1564 (2016).

[22] Q. Zhang, X. He, J. Shi, N. Lu, H. Li, Q. Yu, Z. Zhang, L.-Q. Chen, B. Morris, Q. Xu, P. Yu, L. Gu, K. Jin, and C.-W. Nan, Nat. Commun. **8**, 104 (2017).

[23] B. Cui, P. Werner, T. Ma, X. Zhong, Z. Wang, J. M. Taylor, Y. Zhuang, and S. S. P. Parkin, Nat. Commun. **9**, 3055 (2018).

[24] See Supplemental Material at http://link.aps.org/supplemental/10.1103/PhysRevLett.129.235701 for method description and additional results on XPCS, AFM, and XANES as well as DFT and Quantum Monte Carlo calculations, which includes Refs. [23–52].

[25] S. O. Hruszkewycz, M. Sutton, P. H. Fuoss, B. Adams, S. Rosenkranz, K. F. Ludwig, W. Roseker, D. Fritz, M. Cammarata, D. Zhu, S. Lee, H. Lemke, C. Gutt, A. Robert, G. Grübel, and G. B. Stephenson, Phys. Rev. Lett. **109**, 185502 (2012).

[26] S. O. Hruszkewycz, M. V. Holt, C. E. Murray, J. Bruley, J. Holt, A. Tripathi, O. G. Shpyrko, I. McNulty, M. J. Highland, and P. H. Fuoss, Nano Lett. **12**, 5148 (2012).

[27] S. O. Hruszkewycz, M. J. Highland, M. V. Holt, D. Kim, C. M. Folkman, C. Thompson, A. Tripathi, G. B. Stephenson, S. Hong, and P. H. Fuoss, Phys. Rev. Lett. **110**, 177601 (2013).

[28] Q. Zhang, E. M. Dufresne, and A. R. Sandy, Curr. Opin. Solid State Mater. Sci. **22**, 202 (2018).

[29] G. Brown, P. A. Rikvold, M. Sutton, and M. Grant, Phys. Rev. E **60**, 5151 (1999).

[30] A. R. Sandy, Q. Zhang, and L. B. Lurio, Annu. Rev. Mater. **48**, 167 (2018).

[31] H. A. Tahini, X. Tan, U. Schwingenschlögl, and S. C. Smith, ACS Catal. **6**, 5565 (2016).

[32] Y. Takeda, K. Kanno, T. Takada, O. Yamamoto, M. Takano, N. Nakayama, and Y. Bando, J. Solid State Chem. **63**, 237 (1986).

[33] H. B. Callen and T. A. Welton, Phys. Rev. **83**, 34 (1951).

[34] C. Mitra, T. Meyer, H. N. Lee, and F. A. Reboredo, J. Chem. Phys. **141**, 084710 (2014).

[35] P. R. C. Kent *et al.*, J. Chem. Phys. **152**, 174105 (2020).

[36] J. Kim *et al.*, J. Phys. Condens. Matter **30**, 195901 (2018).

[37] J. T. Krogel, Comput. Phys. Commun. **198**, 154 (2016).

[38] L. Mitáš, E. L. Shirley, and D. M. Ceperley, J. Chem. Phys. **95**, 3467 (1991).

[39] J. T. Krogel and P. R. C. Kent, J. Chem. Phys. **146**, 244101 (2017).

[40] A. L. Dzubak, J. T. Krogel, and F. A. Reboredo, J. Chem. Phys. **147**, 024102 (2017).

[41] N. D. Drummond, R. J. Needs, A. Sorouri, and W. M. C. Foulkes, Phys. Rev. B **78**, 125106 (2008).

[42] L. M. Fraser, W. M. C. Foulkes, G. Rajagopal, R. J. Needs, S. D. Kenny, and A. J. Williamson, Phys. Rev. B **53**, 1814 (1996).

[43] N. D. Drummond, M. D. Towler, and R. J. Needs, Phys. Rev. B **70**, 235119 (2004).

[44] C. J. Umrigar and C. Filippi, Phys. Rev. Lett. **94**, 150201 (2005).

[45] V. I. Anisimov, F. Aryasetiawan, and A. I. Lichtenstein, J. Phys. Condens. Matter **9**, 767 (1997).

[46] V. I. Anisimov, VI, J. Zaanen, and O. K. Andersen, Phys. Rev. B **44**, 943 (1991).

[47] J. P. Perdew and A. Zunger, Phys. Rev. B **23**, 5048 (1981).

[48] P. Giannozzi *et al.*, J. Phys. Condens. Matter **21**, 395502 (2009).

[49] K. Saritas, J. T. Krogel, and F. A. Reboredo, Phys. Rev. B **98**, 155130 (2018).

[50] K. Saritas, J. T. Krogel, S. Okamoto, H. N. Lee, and F. A. Reboredo, Phys. Rev. Mater. **3**, 124414 (2019).

[51] T. K. Andersen, S. Cook, G. Wan, H. Hong, L. D. Marks, and D. D. Fong, ACS Appl. Mater. Interfaces **10**, 5949 (2018).

[52] A. Piovano, G. Agostini, A. I. Frenkel, T. Bertier, C. Prestipino, M. Ceretti, W. Paulus, and C. Lamberti, J. Phys. Chem. C **115**, 1311 (2011).

[53] G. E. Sterbinsky, P. J. Ryan, J.-W. Kim, E. Karapetrova, J. X. Ma, J. Shi, and J. C. Woicik, Phys. Rev. B **85**, 020403(R) (2012).

[54] Q. Zhang, E. M. Dufresne, P. Chen, J. Park, M. P. Cosgriff, M. Yusuf, Y. Dong, D. D. Fong, H. Zhou, Z. Cai, R. J. Harder, S. J. Callori, M. Dawber, P. G. Evans, and A. R. Sandy, Phys. Rev. Lett. **118**, 097601 (2017).

[55] Z. Evenson, B. Ruta, S. Hechler, M. Stolpe, E. Pineda, I. Gallino, and R. Busch, Phys. Rev. Lett. **115**, 175701 (2015).

[56] N. Begam, A. Ragulskaya, A. Girelli, H. Rahmann, S. Chandran, F. Westermeier, M. Reiser, M. Sprung, F. Zhang, C. Gutt, and F. Schreiber, Phys. Rev. Lett. **126**, 098001 (2021).

[57] A. Girelli, H. Rahmann, N. Begam, A. Ragulskaya, M. Reiser, S. Chandran, F. Westermeier, M. Sprung, F. Zhang, C. Gutt, and F. Schreiber, Phys. Rev. Lett. **126**, 138004 (2021).
[58] M. L. Whittaker, D. Ren, C. Ophus, Y. Zhang, L. Waller, B. Gilbert, and J. F. Banfield, Nat. Commun. **13**, 3382 (2022).
[59] E. B. Trigg, L. Wiegart, A. Fluerasu, and H. Koerner, Macromolecules **54**, 6575 (2021).
[60] B. Chung, S. Ramakrishnan, R. Bandyopadhyay, D. Liang, C. F. Zukoski, J. L. Harden, and R. L. Leheny, Phys. Rev. Lett. **96**, 228301 (2006).
[61] S.-W. Chen, H. Guo, K. A. Seu, K. Dumesnil, S. Roy, and S. K. Sinha, Phys. Rev. Lett. **110**, 217201 (2013).
[62] L. Cipelletti, L. Ramos, S. Manley, E. Pitard, D. A. Weitz, E. E. Pashkovski, and M. Johansson, Faraday Discuss. **123**, 237 (2003).
[63] O. J. O'Loan, M. R. Evans, and M. E. Cates, Phys. Rev. E **58**, 1404 (1998).
[64] O. J. O'Loan, M. R. Evans, and M. E. Cates, Europhys. Lett. **42**, 137 (1998).
[65] Y. Nakaye, T. Sakumura, Y. Sakuma, S. Mikusu, A. Dawiec, F. Orsini, P. Grybos, R. Szczygiel, P. Maj, J. D. Ferrara, and T. Taguchi, J. Synchrotron Radiat. **28**, 439 (2021).
[66] T. Zinn, A. Homs, L. Sharpnack, G. Tinti, E. Fröjdh, P.-A. Douissard, M. Kocsis, J. Möller, Y. Chushkin, and T. Narayanan, J. Synchrotron Radiat. **25**, 1753 (2018).
[67] C. G. Schroer, I. Agapov, W. Brefeld, R. Brinkmann, Y.-C. Chae, H.-C. Chao, M. Eriksson, J. Keil, X. Nuel Gavaldà, R. Röhlsberger *et al.*, J. Synchrotron Radiat. **25**, 1277 (2018).
[68] J. Dooling, M. Borland, W. Berg, J. Calvey, G. Decker, L. Emery, K. Harkay, R. Lindberg, G. Navrotksi, V. Sajaev, S. Shoaf, Y. P. Sun, K. P. Wootton, A. Xiao, A. Grannan, and A. H. Lumpkin, Phys. Rev. Accel. Beams **25**, 043001 (2022).
[69] A. Fluerasu, M. Sutton, and E. M. Dufresne, Phys. Rev. Lett. **94**, 055501 (2005).
[70] B. Ruta, Y. Chushkin, G. Monaco, L. Cipelletti, E. Pineda, P. Bruna, V. M. Giordano, and M. Gonzalez-Silveira, Phys. Rev. Lett. **109**, 165701 (2012).
[71] J.-D. Su, A. R. Sandy, J. Mohanty, O. G. Shpyrko, and M. Sutton, Phys. Rev. B **86**, 205105 (2012).
[72] A. Sood, A. D. Poletayev, D. A. Cogswell, P. M. Csernica, J. T. Mefford, D. Fraggedakis, M. F. Toney, A. M. Lindenberg, M. Z. Bazant, and W. C. Chueh, Nat. Rev. Mater. **6**, 847 (2021).
[73] Q. Zhang, E. M. Dufresne, P. Grybos, P. Kmon, P. Maj, S. Narayanan, G. W. Deptuch, R. Szczygiel, and A. Sandy, J. Synchrotron Radiat. **23**, 679 (2016).
[74] A. Koziol, M. Bordessoule, A. Ciavardini, A. Dawiec, P. Da Silva, K. Desjardins, P. Grybos, B. Kanoute, C. Laulhe, P. Maj, C. Menneglier, P. Mercere, F. Orsini, and R. Szczygiel, J. Synchrotron Radiat. **25**, 413 (2018).